Available online at www.sciencedirect.com
SCIENCE DIRECT
Journal of Catalysis 232 (2005) 318–334
JOURNAL OF CATALYSIS
www.elsevier.com/locate/jcat

Evolution of isomorphously substituted iron zeolites during activation: comparison of Fe-beta and Fe-ZSM-5

J. Pérez-Ramírez [a,*], J.C. Groen [b], A. Brückner [c], M.S. Kumar [c], U. Bentrup [c], M.N. Debbagh [d], L.A. Villaescusa [e]

[a] *Laboratory for Heterogeneous Catalysis, Catalan Institution for Research and Advanced studies (ICREA) and Institute of Chemical Research of Catalonia (ICIQ), Av. Països Catalans s/n, E-43007, Tarragona, Spain*
[b] *DelftChemTech, Delft University of Technology, Julianalaan 136, 2628 BL, Delft, The Netherlands*
[c] *Institute for Applied Chemistry Berlin-Adlershof, Richard-Willstätter-Str. 12, D-12484, Berlin, Germany*
[d] *Departamento de Química Inorgánica, Universidad de Alicante, PO Box 99, E-03080, Alicante, Spain*
[e] *Departamento de Química, Universidad Politécnica de Valencia, Camino de Vera s/n, 46071, Valencia, Spain*

Received 12 December 2004; revised 4 March 2005; accepted 23 March 2005

Available online 5 May 2005

Abstract

A number of techniques (ICP-OES, XRD, SEM, ^{27}Al MAS-NMR, N_2 adsorption, NH_3-TPD, FTIR of pyridine adsorbed, HRTEM, UV/vis, and EPR) have been applied to characterize the morphology, structure, porosity, acidity, and forms of iron and aluminum in Fe-beta and Fe-ZSM-5 prepared by hydrothermal synthesis and in their products of activation by calcination and steam treatment. The compositions of the zeolite matrices were very similar, with nominal Si/Al and Si/Fe ratios of 36 and 152, respectively. Removal of the template by calcination leads to extensive dealumination in Fe-beta, while having no influence on the state of aluminum in Fe-ZSM-5. Steam treatment was required to massively create extra-framework Al species in the latter sample. In contrast, the sensitivity of framework iron to migration into non-framework positions during postsynthesis treatments and the nature and distribution of the resulting iron species were remarkably analogous in the two zeolite structures. Catalytic tests with direct N_2O decomposition and N_2O reduction with CO over the steamed iron zeolites confirmed that the microporous matrix intrinsically does not play a decisive role on the activity in these reactions, provided that the resulting forms of iron are similar.

Keywords: Iron zeolites; Fe-beta; Fe-ZSM-5; Characterization; Activation; Calcination; Steaming; Iron species; Acidity; N_2O decomposition; N_2O reduction

1. Introduction

Iron zeolites are active catalysts for a number of reactions, including direct N_2O decomposition [1–3], selective catalytic reduction of NO_x and N_2O [4–7], and selective oxidations of different substrates with (i) N_2O [8–11], (ii) O_2 [12,13], and (iii) H_2O_2 [14,15]. Fe-ZSM-5 has been the most popular zeolite in preparation, characterization, and catalytic studies. Several research groups have investigated the structure–activity relationship of Fe-ZSM-5, particularly the effect of the synthesis procedure on the nature and distribution of iron species and the associated catalytic performance [16–25]. Despite many studies, the structure of the active site(s) in the various applications is still a subject of intense debate and attention.

The most common method of preparing Fe-ZSM-5 is to introduce iron by post-synthetic ion exchange in the solid or liquid phase. A lack of reproducibility of exchange methods in solution has frequently been reported [16,26,27]. Chemical vapor deposition (CVD) of $FeCl_3$ on the zeolite has been suggested as a more reproducible method for preparing over-exchanged Fe-ZSM-5, leading to high iron loadings [4]. A distinct approach consists of inserting iron into

* Corresponding author. Fax: +34 977 920 224.
E-mail address: jperez@iciq.es (J. Pérez-Ramírez).

0021-9517/$ – see front matter
doi:10.1016/j.jcat.2005.03.018

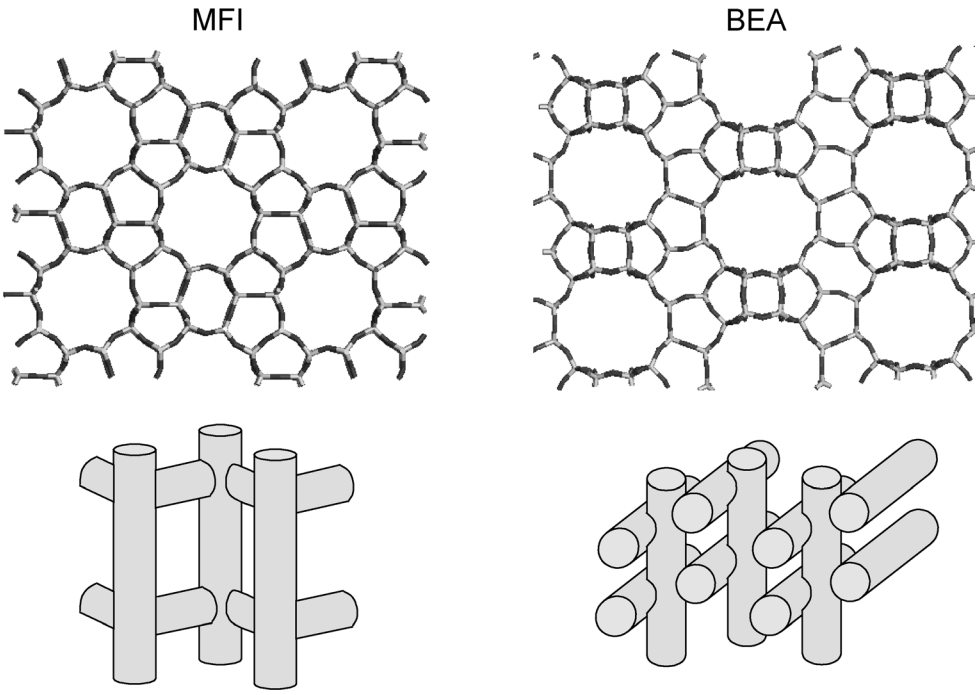

Fig. 1. Structure and pore connectivity in MFI and BEA frameworks.

T positions in the zeolite framework during the hydrothermal synthesis, followed by treatment of the zeolite in air, vacuum, or steam at elevated temperatures [8,10,21,28–33]. These cause the migration of iron to extra-framework positions and their progressive clustering in the form of isolated, dimeric, and polymeric species up to oxidic nanoparticles [29,31,33,34]. The extent of iron extraction and aggregation depends on the activation conditions (atmosphere, temperature) and the composition of the MFI framework [33]. This method is considered a very suitable approach to disperse iron species into the microporous matrix, although typically it does not allow the insertion of high iron content. It has been almost exclusively applied to the synthesis of pentasyl-type Fe-MFI zeolites of various compositions (silicates, titanosilicates, aluminosilicates, gallosilicates, borosilicates, germanosilicates) [33–36].

Steam treatment of isomorphously substituted Fe-ZSM-5 has led to catalysts with high turnover frequencies in direct N_2O decomposition in simulated tail gases from nitric acid plants and combustion processes, as compared with iron zeolites prepared by postsynthesis methods [1,2]. This method has also proved efficient as a way to prepare active catalysts in the reduction of N_2O by CO [23] and in various N_2O-mediated oxidations, like the hydroxylation of benzene to phenol [8–10] or the oxidative dehydrogenation of propane to propylene [11]. Attending to the remarkable catalytic properties of steam-activated Fe-ZSM-5, it is interesting to extrapolate this synthesis route to other microporous matrices, with the intention of obtaining more efficient catalysts for the above applications. Very recently, Berlier et al. [37] synthesized Fe-MCM-22 ($Si/Al = 90$ and $Si/Fe = 18$) by isomorphous insertion and investigated the effect of calcination and treatment in vacuum on the coordination and oxidation changes of iron species. The results obtained were compared with those previously obtained by the same group over Fe-silicalite ($Si/Al = \infty$ and $Si/Fe = 25$–150) [34], although the different compositions of the two zeolites (absence of Al and lower Fe content in Fe-silicalite) make a comparison between the two samples not straightforward. Moreover, the catalytic performance of Fe-MCM-22 sample was not reported.

Zeolite beta appears to be an attractive host for iron, as evident from various works indicating the higher activity of Fe-beta with respect to Fe-ZSM-5 in direct N_2O decomposition [38] and in the selective reduction of N_2O by NH_3 [39] or CH_4 [40]. The effect of the preparation procedure on the iron constitution and performance of Fe-beta has been less extensively explored as compared with Fe-ZSM-5, because it is limited to materials prepared by liquid-ion exchange [41–44]. However, whether the different catalytic performance observed is due to an intrinsic effect of the structural characteristics of the specific zeolite or to the different nature and distribution of the iron species stabilized in both microporous systems remains unclear. Both MFI and BEA structures exhibit multidirectional channel systems (Fig. 1). Zeolite beta is a disordered intergrowth of several hypothetical polymorphs, all characterized by a 3D/12-membered ring channel system, whereas ZSM-5 presents a 3D/10-membered ring channel system. Accordingly, the channel dimensions in beta (0.66×0.67 nm and 0.56×0.57 nm) are larger than those in ZSM-5 (0.53×0.56 nm and 0.51×0.55 nm) [45].

The present work elaborates on the synthesis and characterization of isomorphously substituted Fe-beta and Fe-

ZSM-5 with the same chemical composition and their evolution upon activation by calcination and steam treatments. Parallels and differences between the two microporous matrices have been established with regard to crystal structure, porous characteristics, morphology, acidity, and form(s) of iron and aluminum species. The performance of the steam-activated iron zeolites in direct N_2O decomposition and N_2O reduction by CO was also evaluated to support characterization results and to examine the intrinsic influence of the zeolite matrix on the catalytic activity.

2. Experimental

2.1. Zeolite preparation and activation

Fe-ZSM-5 was synthesized hydrothermally, with tetrapropyl ammonium ions (TPA^+) as the template. Tetraethylorthosilicate (TEOS) was added to the basic solution of TPAOH (20 wt%) and NaOH and allowed to hydrolyze at room temperature. Ethanol produced in the hydrolysis was evaporated, as was a 25% extra weight corresponding to water. The solution obtained was added dropwise to another solution containing the dissolved iron and aluminum nitrates ($Fe(NO_3)_3 \cdot 9H_2O$ and $Al(NO_3)_3 \cdot 9H_2O$). Nominal molar ratios were $TPAOH/Si = 0.1$, $NaOH/Si = 0.2$, $H_2O/Si = 45$, $Si/Al = 36$, and $Si/Fe = 152$. The gel was then transferred to a stainless-steel autoclave lined with Teflon and kept in a static air oven at 448 K for 5 days. The solid was filtered, washed, dried at 353 K, and calcined in static air according to the program: heated from room temperature to 673 K at 3 K min^{-1} and kept isothermal for 3 h, further increased to 823 K at 1.5 K min^{-1} and kept isothermal for 3 h, and cooled to room temperature. The resulting zeolite in the Na-form was converted into the H-form by three consecutive exchanges with an ammonium nitrate solution (0.1 M) overnight and calcined at 823 K as described above.

Fe-beta was synthesized hydrothermally, with tetraethyl ammonium ions (TEA^+) as the template and fluoride anions as the mineralizing agent. The procedure was as follows: $Al(NO_3)_3 \cdot 9H_2O$ and $Fe(NO_3)_3 \cdot 9H_2O$ were dissolved in a solution of TEAOH (17 wt%). Then TEOS was added and allowed to hydrolyze at room temperature. Ethanol produced during the hydrolysis was evaporated, as was some water. Finally, HF (48 wt%) was added to the paste and homogenized by hand. The nominal molar ratios were $TEAOH/Si = 0.61$, $F/Si = 0.5$, $H_2O/Si = 7.5$, $Si/Al = 36$, and $Si/Fe = 152$. The gel was heated in a Teflon-lined steel autoclave at 423 K for 10 days under static conditions. The solid was filtered, washed, dried at 353 K, and calcined with the same program as for Fe-ZSM-5.

Steam activation was carried out at ambient pressure by heating of the calcined zeolites (0.1 g) in a flow of 30 ml STP min^{-1} of N_2 to 873 K at a rate of 2 K min^{-1}, followed by exposure to a mixture of 30 vol% H_2O in N_2 (30 ml STP min^{-1}) for 5 h. Afterward, the sample was cooled in flowing N_2 at a rate of 2 K min^{-1}.

The as-synthesized, calcined, and steamed zeolites are designated here by the prefixes as-, c-, and s-, respectively.

2.2. Characterization methods

Chemical composition of the samples was determined by ICP-OES (Perkin-Elmer Plasma 40 (Si) and Optima 3000DV (axial)).

Powder X-ray diffraction patterns were measured in a Philips X'Pert diffractometer with Bragg–Brentano geometry and Cu-K_α radiation ($\lambda = 0.1541$ nm). Data were collected in the 2θ range of 5–55°, with a step size of 0.02° and a counting time of 5 s.

Scanning electron microscopy images were recorded at 5 kV in a JEOL JSM-6700F field-emission microscope. Samples were coated with palladium to create contrast.

^{27}Al magic-angle spinning (MAS) nuclear magnetic resonance was recorded at 79.5 MHz with a Varian VXR-400S spectrometer. The narrow-bore magnet (50 mm) was fitted with a high-speed MAS Doty probe. The samples were spun in 4-mm-diameter rotors made of zirconia. The length of the r.f. pulses was 0.5 μs, and the spinning frequency was 8.0 kHz. The acquisition time was 0.2 s. A time interval of 1 s between successive accumulations was selected to avoid saturation effects. The number of accumulations (10,000) allowed a signal-to-noise ratio of > 20. The ^{27}Al chemical shift was referenced to $Al(H_2O)_6^{3+}$.

N_2 adsorption at 77 K was carried out in a QuantaChrome Autosorb-6B apparatus. Samples were previously evacuated at 623 K for 16 h. The micropore volume and the mesopore surface area were determined with the t-plot method [46]. The BET method [47] was used to calculate the total surface area of the samples, which is used for comparative purposes.

Temperature-programmed desorption of ammonia was carried out on a Micromeritics TPR/TPD 2900 equipped with a thermal conductivity detector (TCD). The sample (35 mg) was pretreated at 823 K in He (30 ml min^{-1}) for 1 h. Afterward, pure NH_3 (40 ml min^{-1}) was adsorbed at 473 K for 15 min. Subsequently a flow of He (30 ml min^{-1}) was passed through the reactor for 30 min to remove weakly adsorbed ammonia on the zeolite. This procedure was repeated three times. Desorption of NH_3 was monitored in the range 473 to 823 K at 10 K min^{-1}.

The surface acidity of the Fe-zeolites was studied by FTIR spectroscopy of adsorbed pyridine. Spectra were recorded with a Bruker IFS 66 spectrometer equipped with a heatable and evacuable reaction cell with CaF_2 windows, which was connected to gas-dosing and evacuation systems. The zeolite powder was pressed into self-supporting wafers with a diameter of 20 mm and a weight of 50 mg. Before pyridine adsorption, the samples were pretreated in flowing air at 673 K for 1 h, followed by cooling to 373 K. Then pyridine was adsorbed at 373 K for 1 h with bubbling of the Ar flow through a pyridine-containing saturator. Physically

adsorbed pyridine in the sample was evacuated for 5 min at 373 K, and infrared spectra were recorded at different temperatures in the range of 373–673 K with 2 cm^{-1} resolution and 100 scans. The relative concentrations of Brønsted and Lewis acid sites were determined from the area of the absorption bands at 1545 and 1450 cm^{-1}, respectively.

High-resolution transmission electron microscopy was carried out on a Philips CM30UT electron microscope with a field emission gun as the source of electrons, operated at 300 kV. We mounted the samples on Quantifoil carbon polymer supported on a copper grid by placing a few droplets of a suspension of ground sample in ethanol on the grid, followed by drying at ambient conditions. The zeolites were typically amorphized by the electron beam to enhance the visibility of the small iron oxide particles.

Diffuse-reflectance UV/vis spectra were measured at 293 K with a Cary 400 spectrometer (Varian) equipped with a Praying Mantis sample stage from Harrick. To reduce light absorption, samples were diluted with α-Al_2O_3 (previously calcined at 1473 K for 4 h) in a volumetric ratio of 1:3. Deconvolution of the UV/vis spectra into individual bands was performed according to the procedure detailed in [23]. In situ measurements were carried out in a heatable reaction chamber equipped with a temperature programmer and a gas-dosing system with mass-flow controllers. Reduction and reoxidation experiments were performed at 773 K for 1 h in a flow (10 ml min^{-1}) of 20 vol% H_2 in Ar and air, respectively.

Electron paramagnetic resonance spectra were recorded in X-band ($\nu \approx 9.5$ GHz) with the cw spectrometer ELEXSYS 500-10/12 (Bruker) at 293 K and 77 K. The magnetic field was measured with respect to the standard 2,2-diphenyl-1-picrylhydrazyl hydrate (DPPH). The microwave power was 6.3 mW. A modulation frequency of 100 kHz and an amplitude of 0.5 mT were applied.

2.3. Catalytic tests

Activity measurements was carried out in a fixed-bed quartz reactor (4 mm i.d.), with 50 mg of catalyst (125–200 μm) for a space time of 3×10^5 g s mol^{-1} at a total pressure of $P = 1$ bar. The space time is defined as the ratio W/F^0 (N_2O), where W is the catalyst mass and F^0 (N_2O) is the molar flow of N_2O at the reactor inlet. Steady-state performance was measured in the temperature range of 675–850 K at intervals of 25 K in up and down cycles. Feed mixtures of 1.5 mbar N_2O in He (direct N_2O decomposition) or 1.5 mbar N_2O and 1.5 mbar CO in He (N_2O reduction by CO) were applied. Before the tests, the samples were pretreated in the feed mixture at 723 K for 1 h and cooled in that gas flow to the initial reaction temperature. Reactant and product gases were analyzed with an online gas chromatograph (HP 6890) equipped with a thermal conductivity detector, with the use of a Poraplot Q column (for N_2O and CO_2 separation) and a Molsieve 13X column (for N_2, O_2, and CO separation).

Table 1
Chemical composition of the as-synthesized iron zeolites

Sample	Molar metal ratios				Metal content in solid (wt%)		
	Nominal		In solid		Si	Al	Fe
	Si/Al	Si/Fe	Si/Al	Si/Fe			
as-Fe-ZSM-5	36	152	31.7	129	40.8	1.24	0.63
as-Fe-beta	36	152	31.6	135	42.2	1.28	0.62

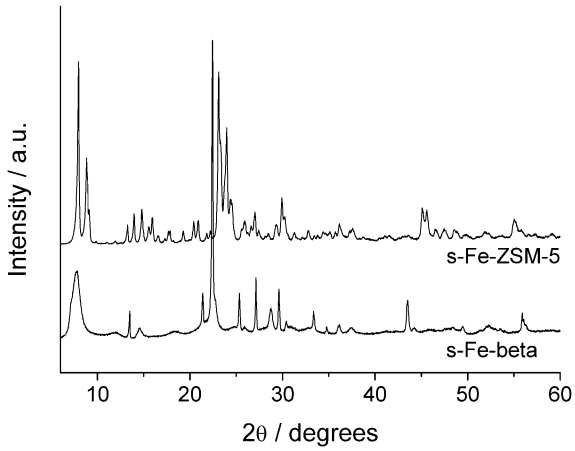

Fig. 2. X-ray diffraction of the steamed Fe-zeolites.

3. Results and discussion

3.1. Chemical composition, XRD, and SEM

Table 1 shows the chemical composition of the as-synthesized Fe-beta and Fe-ZSM-5 zeolites. The values obtained in the solids were very similar to the nominal values in the synthesis gels and, as expected, did not experience significant changes upon calcination and steam treatment. The two zeolites have very similar Si/Al ratios and iron contents, which permits a direct comparison of the physicochemical characterization and catalytic performance. The concentration of Na in the calcined and steamed iron zeolites was below the detection limit of the technique (< 0.01 wt%).

The crystal structure of Fe-ZSM-5 and Fe-beta upon calcination and steam treatment was maintained, and no evidence of any phase other than beta or ZSM-5 was found in the XRD patterns of the various samples, as exemplified by the steamed zeolites in Fig. 2. Likewise, no apparent change in crystal morphology was observed due to the postsynthesis treatments in the SEM micrographs of the as-synthesized, calcined, and steamed Fe-zeolites. Fig. 3 compares crystal sizes and morphologies of the steam-treated s-Fe-beta and s-Fe-ZSM-5 samples. The typical intergrowth phenomenon is clearly distinguished in the ZSM-5 sample, and the beta sample shows truncated bipyramid crystals, characteristic of the synthesis route in fluoride medium, with TEA^+ as the template [48]. The crystal size distribution in both samples is rather uniform, and no amorphous matter was detected at the external surface. The Fe-beta crystals (5 μm) were ca.

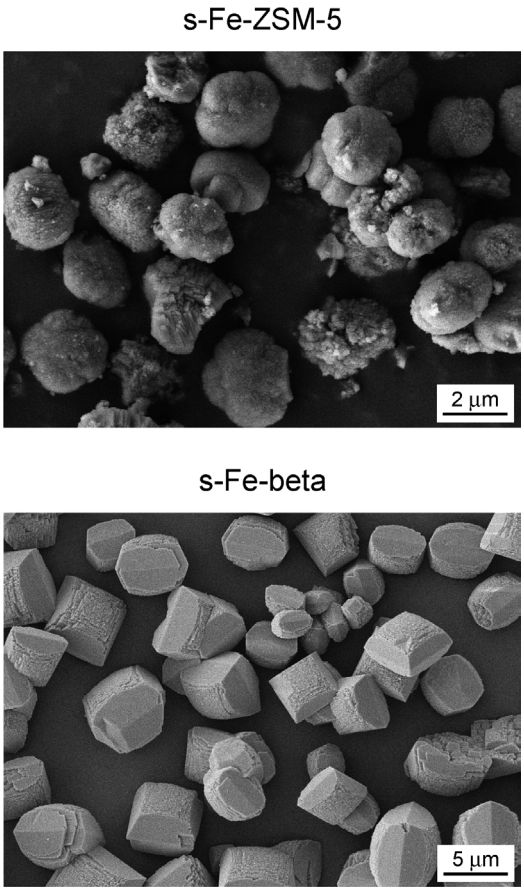

Fig. 3. Field-emission SEM of the steamed Fe-zeolites.

2 times larger than the Fe-ZSM-5 crystals (2.5 µm). Some of the particles in s-Fe-ZSM-5 consist of agglomerates of smaller crystals.

3.2. ^{27}Al MAS-NMR

^{27}Al MAS-NMR spectroscopy was conducted to investigate the changes in aluminum coordination in the zeolites upon calcination and steam treatment (Fig. 4). The spectra of the as-synthesized as-Fe-ZSM-5 and as-Fe-beta samples exhibit a sharp resonance at 55 ppm, which is characteristic of tetrahedrally coordinated Al atoms in lattice positions [49]. The peaks in the region of −25 and 125 ppm are attributed to spinning side bands caused by quadrupole interactions of ^{27}Al nuclei at the spinning frequency applied, which make spectral quantification unfeasible. The shape and intensity of the broad peaks at −25 ppm differ from those at 125 ppm; the former were broader and more intense for both as-synthesized samples. This may suggest the presence of Al in extra-framework positions (EFAl), which normally appears around 0 ppm [49]. Although spinning side bands are not necessarily symmetrical and their relative areas may differ [49], the lack of incorporation of a (minor) fraction of aluminum in the zeolite framework of the as-synthesized samples cannot be completely discarded from our current spectra. However, with careful synthesis procedures and the Si/Al ratio applied, all of the aluminum is expected to occupy framework positions.

The NMR spectra in Fig. 4 make it possible to properly assess the relative susceptibility of Fe-ZSM-5 and Fe-beta for dealumination upon post-treatment. Template removal

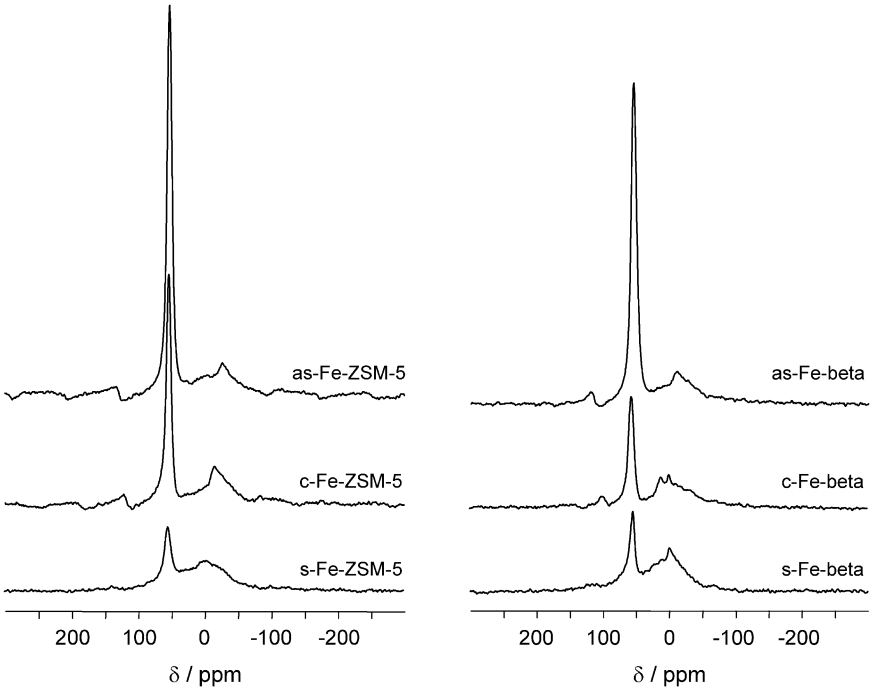

Fig. 4. ^{27}Al MAS-NMR spectra of the as-synthesized, calcined, and steamed Fe-zeolites.

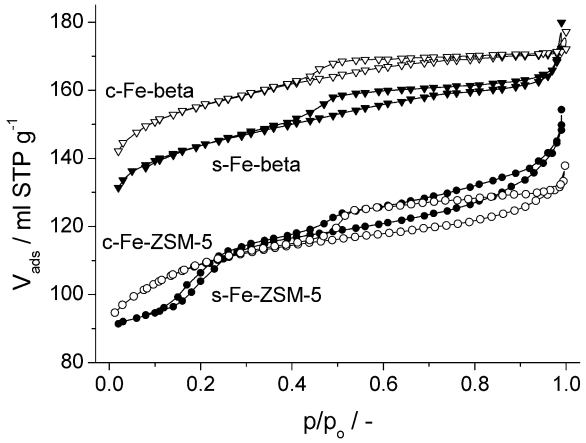

Fig. 5. N_2 adsorption isotherms of the calcined and steamed Fe-zeolites.

by thermal treatment in air induces an important decrease in the relative contribution of tetrahedral Al in the samples (especially in c-Fe-beta), leading to a certain dislodgement of lattice Al species to extra-framework positions. This is also suggested by the distinction of two peaks in the 0 ppm region of c-Fe-beta, which do not appear in c-Fe-ZSM-5. This result indicates the lower stability of lattice aluminum in BEA than in MFI, in agreement with previous studies [50]. The low stability of Al in the BEA framework has been mainly attributed to the number of T-atoms in four-rings (75%), with half of them even connected to two four-rings. In contrast, the MFI framework has only 17% of its T-atoms in four-rings, making them very stable against dealumination. The intrinsic framework flexibility of beta and the presence of stacking faults (increasing the number of defect sites) make this structure prone to dealumination [50].

The resonance at 55 ppm in the steamed zeolites is further decreased, particularly for Fe-ZSM-5, where the Al coordination was relatively insensitive to calcination. The relative intensity of the sharp resonance at 55 ppm and the broad resonance at 0 ppm are comparable in s-Fe-beta and s-Fe-ZSM-5, indicating an extensive degree of dealumination. It should be kept in mind that the decreased intensity of the NMR resonances upon calcination and steaming is due not only to the dislodgement of framework aluminum, but also to the dislodgement of framework iron, which dampens the Al signal because of its paramagnetic effect. The presence in the steamed samples of a broad feature and multiple peaks in the region around 0 ppm does not make it possible to assess the nature of the EFAl species formed. Evidently, the spectra of the steamed samples showed no spinning side bands, and the broadening of this signal is plausibly due to the presence of non-framework Al species with different coordinations and positions. For instance, the resonance at 30 ppm (present in c-Fe-beta and s-Fe-beta) has been attributed to pentacoordinated or highly distorted tetrahedral EFAl species [51–53], and the narrow distribution at 0 ppm has been assigned to framework-connected octahedral Al species [54,55], which can be reinserted at specific T-sites of the framework [56].

Table 2
Textural properties of the calcined and steamed iron zeolites

Sample	V_{micro} [a] ($cm^3\,g^{-1}$)	V_{total} ($cm^3\,g^{-1}$)	S_{meso} [a] ($m^2\,g^{-1}$)	S_{BET} [b] ($m^2\,g^{-1}$)
c-Fe-ZSM-5	0.17	0.21	23	410
s-Fe-ZSM-5	0.16	0.23	33	380
c-Fe-beta	0.21	0.27	23	600
s-Fe-beta	0.19	0.27	28	560

[a] t-plot method.
[b] BET method.

3.3. N_2 adsorption

Nitrogen adsorption was performed to investigate the porous properties of the calcined zeolites and the changes therein upon steam treatment. The N_2 isotherms of the calcined zeolites in Fig. 5 exhibit high nitrogen uptakes at low relative pressures and a plateau at high relative pressures, which is typical for microporous materials (type I according to IUPAC classification [57]). Application of the BET model and the t-plot method confirms that the majority of the surface area ($S_{BET} = 410$ and 600 $m^2\,g^{-1}$ for c-Fe-ZSM-5 and c-Fe-beta, respectively) is due to the presence of micropores, whereas the contribution of mesoporosity is relatively small ($S_{meso} = 23\ m^2\,g^{-1}$). Although the validity of the BET model for highly microporous materials is questionable, the surface areas derived from this model in the adapted pressure range $p/p_0 = 0.01$–0.10 can still be used for comparative purposes [58]. As shown in Table 2, the micropore volume of c-Fe-beta is higher than that of c-Fe-ZSM-5, as expected from the more open framework structure of the former zeolite (cf. Fig. 1). Upon steam treatment, only slight changes in the uptake of N_2 at pressures $p/p_0 > 0.4$ were observed, which can be attributed to the formation of a limited mesoporosity as a consequence of the extraction of heteroatoms (Al and Fe) to non-framework positions. This is further supported by a certain increase in the mesopore area in the steamed samples (Table 2). Simultaneously, the micropore volume decreases slightly (5–10%), as indicated by the decreased uptake at low pressure and the application of the t-plot. The closure of the hysteresis loop around $p/p_0 = 0.5$ present for all of the samples is due to the well-known tensile strength effect of the adsorptive, and does not represent any physical porosity at this particular relative pressure [59]. The substep observed in the isotherm of s-Fe-ZSM-5 around $p/p_0 = 0.2$ is a particular feature of MFI-type zeolites and is associated with a fluid-to-solid-like phase transition of the adsorbed N_2 in the microporous network and consequently should not be attributed to the formation of additional (meso)porosity [59]. This substep generally becomes more pronounced as the framework Si/Al ratio increases, which indirectly substantiates the dislodgement of framework aluminum upon steam treatment of c-Fe-ZSM-5, as concluded from NMR.

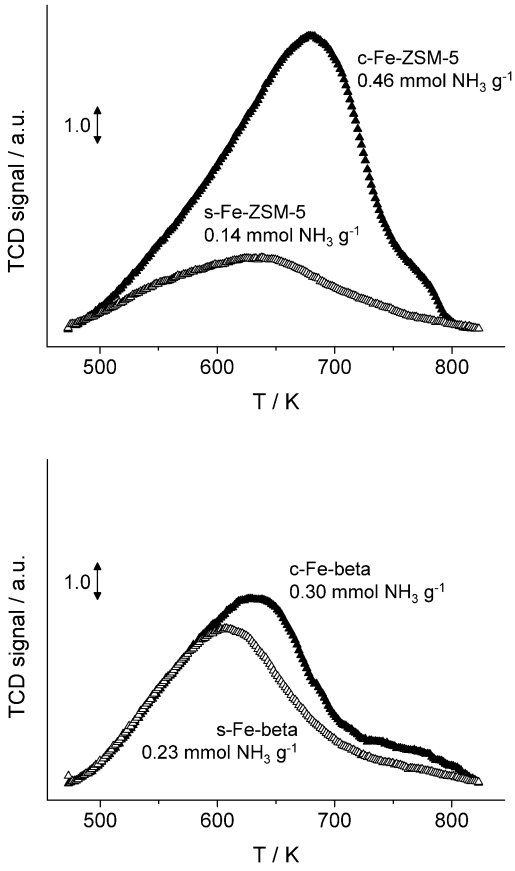

Fig. 6. NH_3-TPD profiles of the calcined and steamed Fe-zeolites. The ammonia uptake is included in the figure.

3.4. NH_3-TPD

Temperature-programmed desorption of ammonia has been widely applied to obtain the density of Brønsted acids in zeolites. However, an important drawback of this technique is that adsorption of ammonia is not specific to Brønsted acid sites [60]. Adsorption on non-Brønsted acid sites (referred to as Lewis acid sites) may be stronger than that on Brønsted sites. In this respect, Juskelis et al. [61] demonstrated that ammonia adsorbs more strongly on CaO than it does on USY zeolite. Taking this into consideration, the NH_3 desorption profiles shown in Fig. 6 cannot be simply applied for a definitive assignment of the desorbed ammonia to Brønsted and Lewis acid sites. However, they provide a valuable fingerprint of the overall nature and distribution of the acid sites (weak or strong) in the calcined and steamed Fe-ZSM-5 and Fe-beta zeolites, and a quantification of the density of total acid sites. This technique is particularly useful when it is complemented by FTIR spectroscopy of adsorbed pyridine; the latter is able to discriminate between different acid sites (Section 3.5).

The strength of the acid sites in c-Fe-ZSM-5 is slightly higher than that in c-Fe-beta, as indicated by the position of the maximum at 690 and 630 K, respectively. The total NH_3 uptake in c-Fe-ZSM-5 (0.46 mmol g^{-1}) is also higher than in c-Fe-beta (0.30 mmol g^{-1}), despite the nearly identical Si/Al ratios in the two samples (Table 1). The lower density of acid sites in c-Fe-beta as compared with c-Fe-ZSM-5 can be confidently attributed to the higher degree of Al extraction in c-Fe-beta, as indicated by ^{27}Al MAS-NMR, which contrasts with the relative inertness of framework aluminum upon calcination of as-Fe-ZSM-5.

Steam treatment of c-Fe-ZSM-5 dramatically decreases the strength and number of acid sites in the zeolite, indicating that most of the acid sites in the calcined sample are Brønsted-type; that is, they arise from the presence of Al and Fe in the framework. In contrast, only slight changes are observed in the NH_3 desorption profile upon steaming of c-Fe-beta. This suggests that after the major dealumination occurring during calcination of as-Fe-beta, subsequent steam treatment of c-Fe-beta does not significantly affect the Al coordination (as suggested by NMR), and, expectedly, the adsorption properties of c-Fe-beta and s-Fe-beta hardly changed either. As a result, the total NH_3 uptake in s-Fe-beta is higher than that in s-Fe-ZSM-5.

Extraction of one iron atom by the cleavage of a Si–O(H)–Fe bond will have an effect on the NH_3-TPD profile equivalent to that of the extraction of one aluminum atom by the cleavage of a Si–O(H)–Al bond. As a matter of fact, Gorte [60] concluded that Brønsted acid sites in H-[Fe]MFI are very similar to those in H-[Al]MFI, regardless of the probe molecule applied (NH_3, pyridine, and acetonitrile). However, so far the acidity changes have been discussed in light of the ^{27}Al MAS-NMR characterization, principally because of the significantly higher amount of aluminum as compared with iron in the samples (molar Al/Fe ratio ≈ 4). The suitability of this approach is further discussed in later sections.

3.5. FTIR of pyridine adsorbed

FTIR of adsorbed pyridine was conducted to elucidate the nature and relative amounts of the Brønsted and Lewis acid sites in the calcined and steamed iron-containing zeolites, complementing the previous NH_3-TPD results. Generally, bands around 1540–1548 and 1445–1460 cm^{-1} are characteristic of Brønsted (PyH^+) and Lewis (L-Py) acid sites, respectively. Moreover, bands of hydrogen-bonded pyridine (hb-Py) are expected in the range of 1440–1447 and 1580–1600 cm^{-1}, and bands of physically adsorbed pyridine (ph-Py) are expected at 1439 and 1580 cm^{-1} [62–64]. Based on these assignments, the discrimination between Lewis-bonded and hydrogen-bonded pyridine is not possible in principle. However, the thermal stability of the adsorbed pyridine species differs, increasing in the order ph-Py < hb-Py < L-Py, PyH^+. Accordingly, Lewis-bonded pyridine can be properly determined from a record of the infrared spectra at sufficiently high temperatures [65], to accomplish complete desorption of hb-Py (vide infra).

The infrared spectra of the various samples at 373 K are shown in Fig. 7. The bands at 1545 cm^{-1} are attributed to

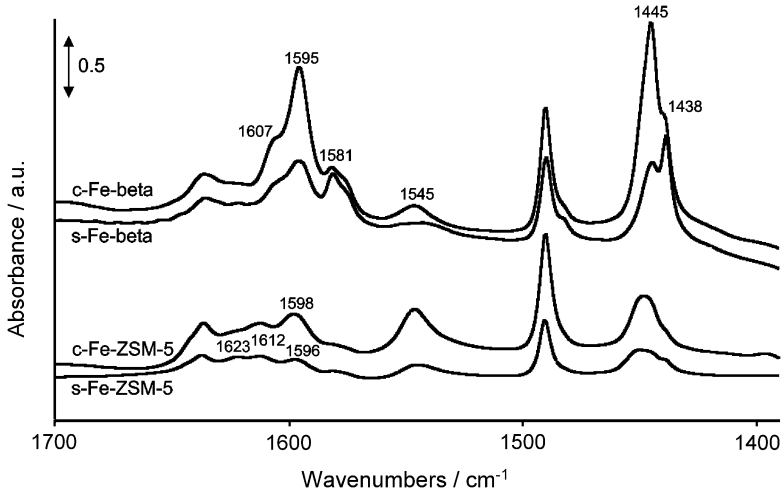

Fig. 7. FTIR spectra of pyridine adsorbed on various Fe-zeolites at 373 K. Background spectra of the air-pretreated samples were subtracted.

Table 3
Areas (in arbitrary units) of the absorption bands in the FTIR spectra at 523 K of pyridine adsorbed associated with Brønsted (PyH^+) and Lewis (L-Py) acidity and the corresponding ratio

Sample	PyH^+, 1545 cm^{-1}	L-Py, 1445 cm^{-1}	PyH^+/L-Py
c-Fe-ZSM-5	5.3	1.2	4.4
s-Fe-ZSM-5	1.0	1.1	0.9
c-Fe-beta	4.0	4.5	0.9
s-Fe-beta	2.7	1.1	2.4

Brønsted acidity, and the bands around 1445 cm^{-1} comprise pyridine adsorbed on Lewis acid sites and hydrogen-bonded pyridine. The band at 1438 cm^{-1} is due to physically adsorbed pyridine. Bands around 1600 cm^{-1} are also due to pyridine adsorbed on Lewis sites and can be considered a measure of the Lewis acid strength of the surface sites [62]. The assignment of the band at 1623 cm^{-1} observed in the spectrum of s-Fe-ZSM-5 is controversial. Buzzoni et al. [64] assigned it to Brønsted acidity in zeolites, whereas Busca et al. [62] attributed it to Al Lewis acid sites of γ-Al_2O_3 and amorphous Al_2O_3/SiO_2 samples.

The ratio of Brønsted to Lewis acid sites was estimated from the area of the bands at 1545 cm^{-1} (PyH^+) and 1445 cm^{-1} (L-Py), respectively, since the ratio of the extinction coefficients of these two absorption bands is ~ 1 [66–69]. As shown in Table 3, this ratio depends on the zeolite type and its corresponding treatment. To exclude the influence of hb-Py, which results in an overestimated Lewis acidity, the bands in the spectra at 523 K were used for quantification. At this temperature, the hb-Py is completely removed, as clearly illustrated by the desorption spectra of s-Fe-ZSM-5 and s-Fe-beta, which we obtained by heating the samples in the range of 373–673 K at 10 K min^{-1} (Fig. 8). The total density of acid sites (the sum of total Brønsted and Lewis acid sites) was decreased by 68% from c-Fe-ZSM-5 to s-Fe-ZSM-5, in excellent agreement with the 70% determined from NH_3-TPD. Unexpectedly, quantification from the two techniques did not match as perfectly from c-Fe-beta to s-Fe-beta (55% acidity decrease by pyridine adsorption and only 23% by NH_3-TPD).

With regard to the intensity of the infrared band at 1545 cm^{-1} in Fig. 7, c-Fe-ZSM-5 contains the highest density of Brønsted acid sites, originating from the excess of negative charge as a consequence of the isomorphous substitution of trivalent cations such as Al^{3+} and Fe^{3+} for Si^{4+}. Extraction of the latter heteroatoms to extra-framework positions causes a decrease in the number of Brønsted acid sites. In agreement with NH_3-TPD, the Brønsted acidity in c-Fe-beta is significantly lower than that in c-Fe-ZSM-5, because of the relatively higher degree of dealumination of Fe-beta during calcination. A pronounced decrease in Brønsted sites is observed upon steaming of c-Fe-ZSM-5, as denoted by the reduced intensity of the band at 1545 cm^{-1} in s-Fe-ZSM-5 in Fig. 7 and Table 3. This effect is less pronounced in Fe-beta. These observations are in excellent agreement with results from NH_3-TPD and ^{27}Al MAS-NMR.

In addition to dealumination, the activation of the as-synthesized zeolites by calcination and steaming induces dislodgment of framework iron ions. As noted earlier, this should contribute to the acidity differences observed, despite the lower Fe content as compared with Al. The lower total intensity observed in the Lewis band region of s-Fe-ZSM-5 and s-Fe-beta as compared with c-Fe-ZSM-5 and c-Fe-beta can be related to the process of iron and aluminum extraction and clustering upon steam treatment. The so-formed oxidic species may cause a certain blockage of micropores, as suggested by the slight decrease in V_{micro} in Table 2, possibly leading to hindered diffusion of pyridine through the zeolite pores.

Fig. 9 displays the FTIR band area for pyridinium ions (PyH^+) at 1545 cm^{-1} and for pyridine coordinated to Lewis acid sites (L-Py) at 1445 cm^{-1} in the calcined and steam-treated zeolites as a function of the desorption temperature. The number of Lewis sites decreases markedly below 450–500 K and moderately above these temperatures. This dependence is due to the significant contribution of hydrogen-

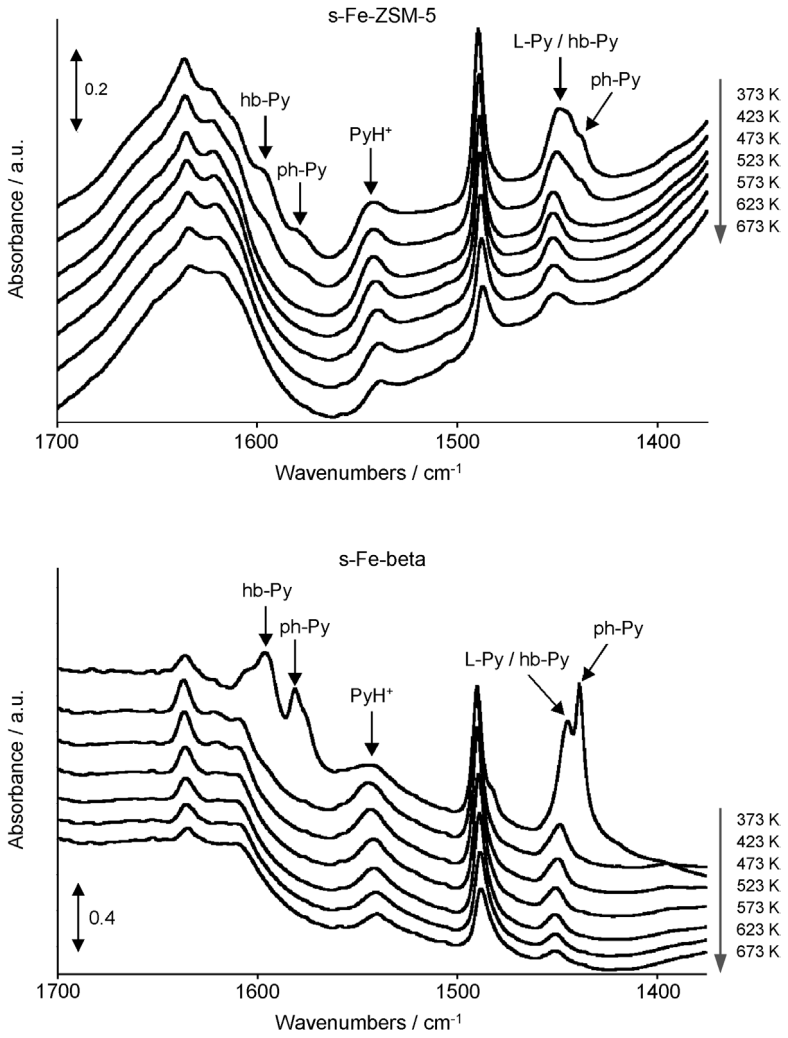

Fig. 8. FTIR spectra of pyridine adsorbed on s-Fe-ZSM-5 and s-Fe-beta at different temperatures. Subtraction of background spectra was not applied.

bonded pyridine in the Lewis acidity region < 500 K. The slight increase in Brønsted band intensity between 373 K and 423 K in s-Fe-beta is related to the better availability of these sites at higher temperatures, induced by the dramatic decrease in typical bands related to physically adsorbed and hydrogen-bonded pyridine (Fig. 8). The latter is indicated by the disappearance of the bands at 1438 cm^{-1} and 1580–1595 cm^{-1} at 423 K. In contrast, pyridine adsorbed on Brønsted acid sites and on stronger Lewis sites is more stable. This is expected in the case of Brønsted sites, since removal of pyridine from the former requires decomposition of the adsorbed pyridinium ion. However, the stability of the strong Lewis acid sites, which are still detectable above 500 K, seems to be comparable to that of the Brønsted sites, since the slope of the intensity versus temperature curves is similar for the two types of sites in the two zeolites. This result evidences that Lewis sites can be formed in those zeolites, which are as strong as Brønsted sites. This agrees with findings of Meloni et al. [70], who detected an even higher stability of pyridine adsorbed on Lewis than on Brønsted sites in Fe-silicalite.

3.6. HRTEM

High-resolution transmission electron microscopy was primarily used to investigate the extraction of framework iron and clustering of extra-framework iron species upon calcination and steam treatment. As expected, the HRTEM micrographs of the as-synthesized zeolites in Fig. 10 do not show any separated iron-containing phase, supporting isomorphous substitution of iron in the zeolite framework. Calcination of as-Fe-ZSM-5 induces extraction of framework iron to extra-framework positions, as concluded from the presence of very small iron oxide moieties in the HRTEM micrograph of the c-Fe-ZSM-5 sample. It should be mentioned that these particles were observed in restricted areas of c-Fe-ZSM-5 (in 2 of the 15 spots analyzed throughout the specimen), qualitatively indicating the minor degree of iron clustering in this sample. No iron oxide-like entities were visualized in c-Fe-beta.

Steam treatment massively dislodges framework iron to extra-framework positions, as concluded from the formation of homogenously dispersed iron oxide nanoparticles of 1–

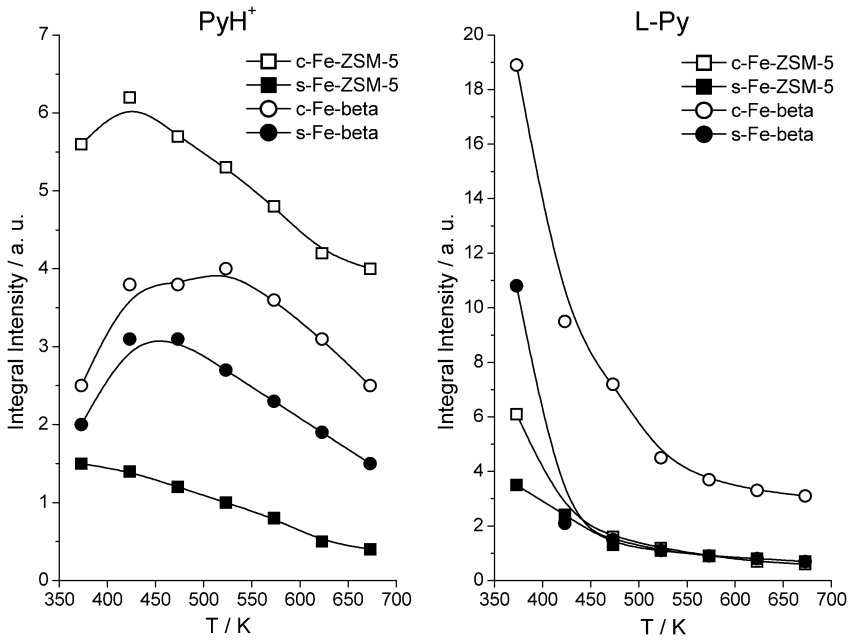

Fig. 9. Change of the FTIR band area for pyridium ions (PyH^+) at 1545 cm^{-1} and for pyridine coordinated to Lewis acid sites (L-Py) at 1445 cm^{-1} vs desorption temperature over the calcined and steamed iron zeolites.

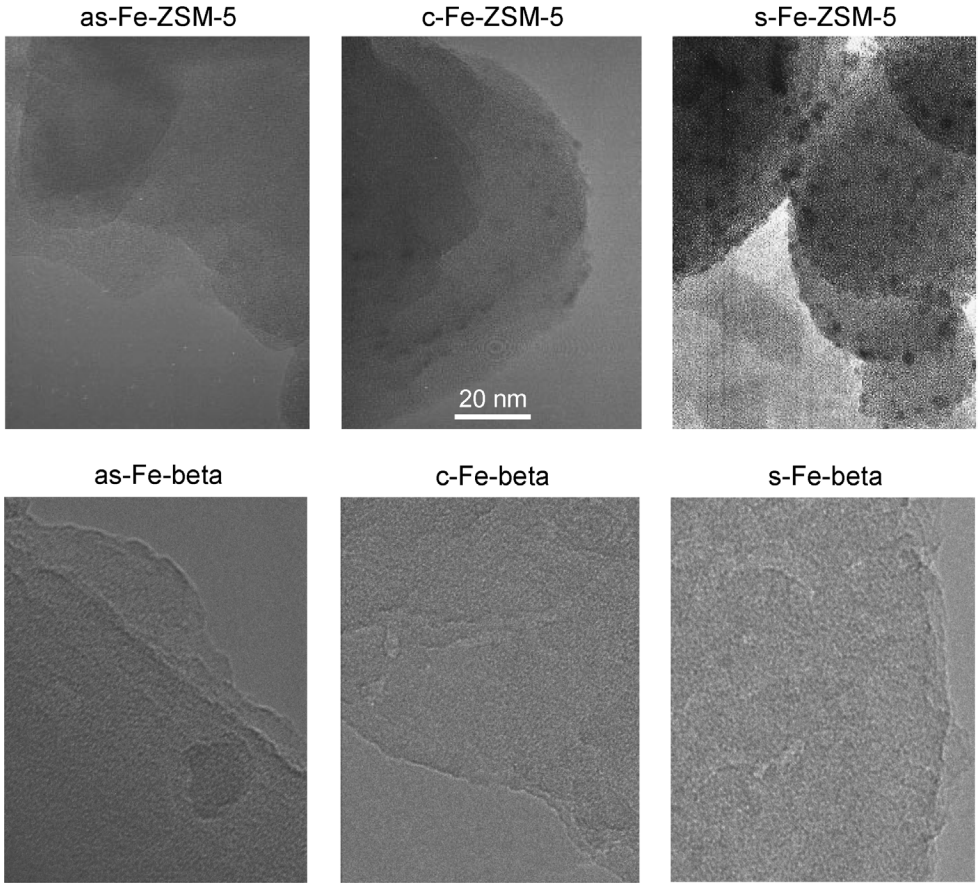

Fig. 10. HRTEM of the as-synthesized, calcined, and steamed Fe-zeolites. The scale bar is the same for all the samples.

Table 4
Percentage of the area of the bands (I_1 at $\lambda < 300$ nm, I_2 at $300 < \lambda < 400$ nm, and I_3 at $\lambda > 400$ nm) derived from deconvolution of the UV/vis spectra in Fig. 11, and corresponding Fe percentage determined from the total iron content of the samples

Sample	I_1[a] (%)	Fe_1 (wt%)	I_2[b] (%)	Fe_2 (wt%)	I_3[c] (%)	Fe_3 (wt%)
as-Fe-ZSM-5	100	0.63	–	–	–	–
c-Fe-ZSM-5	89	0.56	11	0.07	–	–
s-Fe-ZSM-5	51	0.32	34	0.21	15	0.09
as-Fe-beta	100	0.62	–	–	–	–
c-Fe-beta	84	0.52	16	0.09	–	–
s-Fe-beta	47	0.30	36	0.22	17	0.1

[a] Isolated Fe^{3+} in tetrahedral and higher coordination.
[b] Oligonuclear $Fe_x^{3+}O_y$ species.
[c] Fe_2O_3 nanoparticles.

2 nm in s-Fe-ZSM-5. Particles were observed in s-Fe-beta, but to a lesser extent (both in concentration and size) than in s-Fe-ZSM-5. These observations seem to indicate a lower degree of iron agglomeration in s-Fe-beta, which can be associated with (i) a lower degree of extraction of framework iron or (ii) a reduced tendency of the extra-framework iron species to form large aggregates. The latter possibility would imply a better stabilization of small iron-containing species in the pores of beta as compared with ZSM-5. These alternatives cannot be discriminated from by microscopy studies. To further assess the nature and distribution of the iron species in both Fe-ZSM-5 and Fe-beta at the different stages of their preparation and activation, UV/vis and EPR spectroscopies were applied.

Concerning changes in the pore structure of the as-synthesized zeolite upon post-treatments, it should be added that the micrographs of c-Fe-beta and especially s-Fe-beta in Fig. 10 support the formation of extra-mesoporosity upon calcination and steam treatment, in agreement with N_2 adsorption results in Table 2. However, no noticeable change was observed in the post-treated Fe-ZSM-5 samples.

3.7. UV/vis

Diffuse-reflectance UV/vis spectroscopy was used to assess the nature and distribution of Fe(III) species in the zeolites at the different stages of their preparation. As shown in Fig. 11, the measured spectra were converted into Kubelka–Munk functions and deconvoluted into the lowest possible number of Gaussian subbands, following the fitting procedure detailed in [23]. The relative intensities of these subbands are listed in Table 4, including the corresponding percentage of the different Fe^{3+} species. We estimated this by multiplying the relative subband intensities by the total iron content in the zeolites, leading to Fe_1 for isolated Fe^{3+} ions ($\lambda < 300$ nm), Fe_2 for small oligonuclear $Fe_x^{3+}O_y$ clusters in the zeolite channels ($300 < \lambda < 400$ nm), and Fe_3 for Fe_2O_3 nanoparticles at the external surface of the zeolite crystal ($\lambda > 400$ nm).

The quantification of the different Fe species from the below assignments and the area of the corresponding subbands should be taken cautiously a priori, since the absorption coefficients of the various charge-transfer (CT) transitions of iron in these zeolites are unknown. Lehmann [71] determined molar extinction coefficients of CT transitions of isolated Fe^{3+} ions in octahedral and tetrahedral coordination in different solid matrices. For single crystals of aluminum phosphate containing 1 mol% Fe^{3+} in tetrahedral ($AlPO_4$) or octahedral ($AlPO_4 \cdot 2H_2O$) symmetry, similar molar extinction coefficients of 4.55×10^6–4.60×10^6 $l\,cm^{-1}\,mol^{-1}$ for octahedral Fe^{3+} and 1.20×10^6 $l\,cm^{-1}\,mol^{-1}$ for tetrahedral Fe^{3+} were reported. In a recent study, Akl [72] determined absorption coefficients for thin films of amorphous Fe_2O_3 at 477 nm in the range of 0.8×10^5 to 2.7×10^5 cm^{-1}. Multiplication of the molar extinction coefficients provided by Lehmann [71] by the respective Fe^{3+} concentration in the aluminum phosphates (1 mol%, corresponding to 0.1 $mol\,cm^{-3}$) leads to values from 4.55×10^5 to 4.60×10^5 cm^{-1} and 1.20×10^5 cm^{-1} for the CT bands of isolated Fe^{3+} ions in octahedral and tetrahedral coordination, respectively. Comparison of these values with those from CT transitions of Fe_2O_3 by Akl [72] permits us to conclude that the absorption coefficients for CT bands of the various iron species are of the same order of magnitude. Based on these supportive results and our previous experience [23], it is inferred that the data in Table 4 provide a semiquantitative estimate of the distribution of iron species in the zeolites. Furthermore, the comparison for the same type of iron species in different samples should not be influenced by the absorption coefficients, since the position of subbands used is the same in all samples.

Typical *d*–*d* transitions of Fe^{3+}, which are expected between 350 and 550 nm, are symmetry- and spin-forbidden and therefore are not observable in the spectra of Fig. 11. The observed signals are assigned to $Fe^{3+} \leftarrow O$ CT bands. For isolated Fe^{3+} species, two CT bands are expected in the high-energy range of the spectrum (< 300 nm) [34,71,73], whereby their particular position depends on the number of ligands. For regular octahedral symmetry, they arise from the $t_1 \rightarrow t_2$ and $t_1 \rightarrow e$ transitions [73]. Since Fe^{3+} ions in the zeolites likely deviate from regular symmetry, this notation cannot be strictly applied, although it has commonly been used [34,71]. Nevertheless, two CT transitions may also be observed for more or less distorted isolated Fe^{3+} sites. For tetrahedral Fe^{3+} in framework positions of Fe-silicalite they have been observed at 215 and 241 nm [34], and for tetrahedral Fe^{3+} in other matrices they were both found below 250 nm [71]. For octahedral Fe^{3+} in different matrices, those two bands were observed in the ranges of 187–234 nm and 244–305 nm [71,73].

The as-synthesized as-Fe-beta and as-Fe-ZSM-5 samples show one absorption band at 225 and 252 nm, respectively. According to the above considerations, they can be attributed to isomorphously substituted Fe^{3+} sites in tetrahedral positions of the corresponding zeolite lattice. In order to ac-

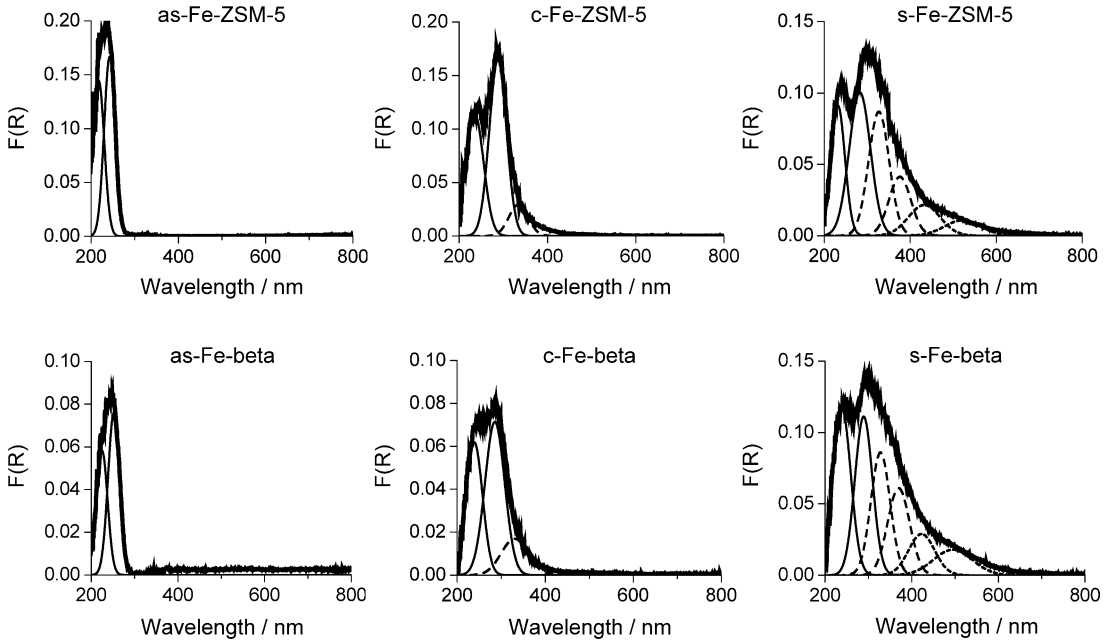

Fig. 11. UV/vis spectra measured at room temperature and deconvoluted bands of as-synthesized, calcined, and steamed Fe-zeolites. Sample c-Fe-beta was obtained by in situ calcination of as-Fe-beta in the UV/vis cell and measured in dehydrated form, while all other samples were measured in hydrated form after long-term storage in ambient atmosphere.

count for the molecular orbital scheme, which predicts two CT transitions for the same isolated Fe^{3+} site [71,73], the experimental spectra of as-Fe-beta and as-Fe-ZSM-5 have been deconvoluted into two subbands falling at 225 and 252 nm. However, it is evident from Fig. 11 that the two CT bands cannot be resolved, because of their small distance and large line width. Thus, a satisfactory fit can also be obtained with the use of one subband for the same isolated Fe^{3+} site only (not shown). Therefore, in the spectra of the calcined and steamed samples that contain other types of Fe^{3+} species in addition to isolated tetrahedral ones, only one subband has been used to fit the maximum at the lowest wavelength. In addition, samples c-Fe-beta and c-Fe-ZSM-5 show a maximum around 285 nm, which is tentatively assigned to isolated, higher coordinated Fe^{3+} species in extra-framework positions. Discrimination between isolated Fe^{3+} ions in tetrahedral and higher coordination has been regarded to be difficult or even impossible so far [23,34]. However, in situ UV/vis measurements given below will show that the subband at 285 nm in hydrated c-Fe-ZSM-5 decreases upon dehydration in air at 773 K in favor of the band at 235 nm (compare Figs. 11 and 12 for c-Fe-ZSM-5), strongly suggesting the release of coordinating water ligands from a part of the Fe species by which the latter obey tetrahedral coordination. This interesting result is a strong experimental justification for the assignment of the UV subbands at 235 and 285 nm to Fe^{3+} ions in tetrahedral and higher coordination, respectively. However, it should be mentioned that the band around 235 nm in the calcined zeolites cannot be exclusively assigned to tetrahedral Fe^{3+} since, as discussed above, octahedral Fe^{3+} species might also contribute to this band. The spectra of the calcined zeolites also display a broad contribution centered at 335 nm (dashed lines in Fig. 11), which is attributed to iron ions in small oligonuclear clusters ($Fe_x^{3+}O_y$) [34]. These results clearly indicate that removal of the template by calcination of the as-synthesized zeolites induces a substantial dislodgment of framework Fe^{3+} ions and even a certain degree of iron association. The contribution of oligonuclear oxo-clusters was estimated at 11 and 16% of all the iron in c-Fe-ZSM-5 and c-Fe-beta, respectively. The absence of a band above 400 nm (dotted lines in Fig. 11) indicates that large Fe_2O_3 particles should not be present in the calcined zeolites [34]. This basically agrees with HRTEM observations, except for the infrequent observation of small iron-containing moieties in c-Fe-ZSM-5 (cf. Fig. 10). It is thus concluded that the number of iron oxide nanoparticles in this sample is too small to be detected by UV/vis.

In general, light absorption in the spectra of Fig. 11 around 335 nm occurs in a very wide range of energy, suggesting the superposition of those bands for oligonuclear Fe_xO_y clusters with various sizes and geometries, even overlapping to some extent with the region of Fe_2O_3 particles (> 400 nm). Accordingly, the minimum number of bands above 300 nm needed to obtain a satisfactory fit of the experimental spectrum has been used for spectra deconvolution.

Steam treatment of c-Fe-beta and c-Fe-ZSM-5 induces further dislodgement of iron from the zeolite framework to extra-framework positions, accompanied by an increased degree of iron clustering. The contribution of oligonuclear iron oxo-clusters increases from 11 and 16% in the calcined zeolites to 34 and 36%, respectively, in the steamed samples (Table 4), and a contribution above 400 nm indicates the presence of large iron oxide particles (15–17% of the overall spectra). These nanoparticles were observed in the micro-

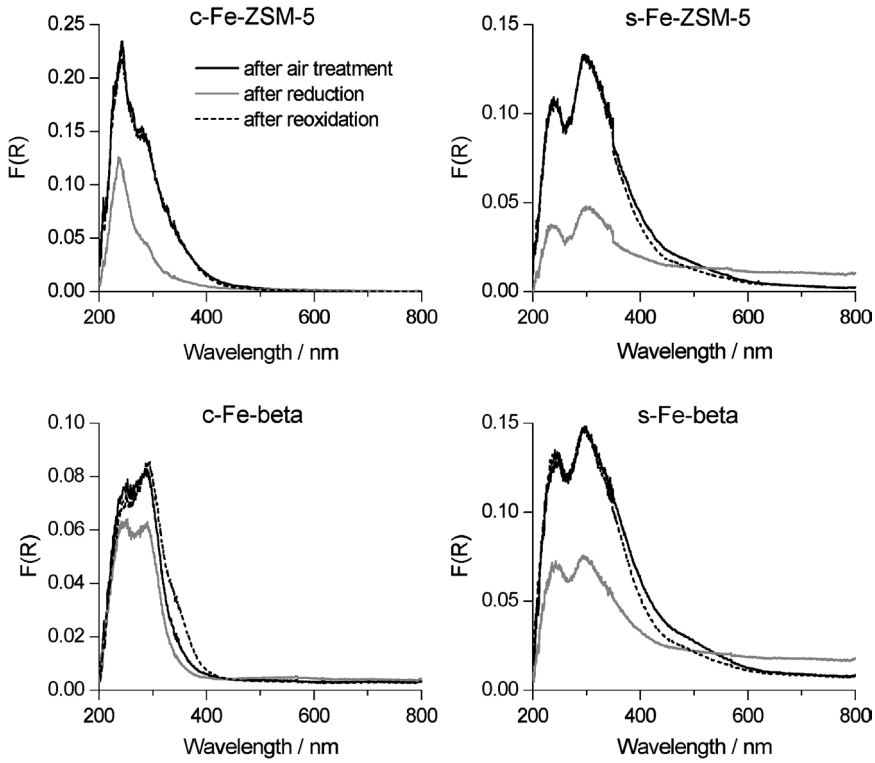

Fig. 12. In situ UV/vis spectra measured at room temperature of the calcined and steamed Fe-zeolites after oxidative pretreatment in flowing air at 773 K for 1 h (solid line), after reduction in 20 vol% H_2 in Ar at 773 K for 1 h (gray line), and after reoxidation in air at 773 K for 1 h (dotted line).

graphs of the steamed samples, particularly in s-Fe-ZSM-5 (Fig. 10).

In summary, the UV/vis results unequivocally indicate that the nature and distribution of the different Fe^{3+} species in c-Fe-ZSM-5 and c-Fe-beta, as well as in s-Fe-ZSM-5 and s-Fe-beta, are very similar. So both the zeolite host and the post-treatment lead to the stabilization of the same forms and distribution of iron species. Based on the high susceptibility of Fe-beta to dealumination, one could expect a higher degree of iron dislodgment and clustering upon calcination with respect to Fe-ZSM-5. However, our results have indicated that the extraction and clustering of iron upon calcination and steaming are alike in the two zeolites. This suggests that the process of formation of extra-framework species depends not only on the zeolite structure, but also on the nature of the trivalent heteroatom. These results also support the conclusion that the different dealumination behavior determines the relative acidity changes observed by NH_3-TPD and FTIR of adsorbed pyridine.

Despite the same iron content, the intensity of the UV/vis signals in the as-synthesized and calcined Fe-ZSM-5 samples is significantly higher than in the corresponding Fe-beta samples, whereas similar intensities are obtained for the steamed zeolites (Fig. 11). At this stage, we cannot provide a definitive explanation for this observation, since it is very unlikely that the presence of divalent iron in the Fe-beta samples accounts for this large difference. Differences in measurement conditions like particle size, packing density in the sample cup, and alignment of the light source may affect the overall intensity of the resulting spectra.

The redox behavior of iron species in the calcined and steamed Fe-ZSM-5 and Fe-beta samples has been further investigated by in situ UV/vis with the use of sequential reductive (20 vol% H_2 in Ar) and oxidative (air) treatments at 773 K. When c-Fe-ZSM-5 is heated in flowing air from room temperature to 773 K, the intensity of the subband at 285 nm decreases in favor of the band around 235 nm (compare related spectra in Figs. 11 and 12). As argued above, this is most probably due to the release of water molecules, which are coordinated to a part of the Fe species. Loss of those ligands transforms higher coordinated Fe ions into tetrahedrally coordinated ones, which contribute to the UV subband around 235 nm. A similar behavior is not evident for the c-Fe-beta sample (compare related spectra in Figs. 11 and 12). However, this is not surprising, since the spectrum of c-Fe-beta in Fig. 11 was recorded after in situ calcination of as-Fe-beta in the UV/vis cell without subsequent rehydration in ambient atmosphere. Differently, c-Fe-ZSM-5 was stored in ambient atmosphere for several months.

Reduction in H_2/Ar flow at 773 K leads to a decrease in UV/vis band intensity in the calcined and steamed zeolites due to the reduction of Fe^{3+} species. Since framework iron ions were found not to be reducible under these conditions [23], the decreased intensity in the calcined samples is attributed to isolated Fe^{3+} ions in extra-framework positions. In the steamed zeolites, the fraction of reducible iron(III) sites is much higher than in the calcined zeolites

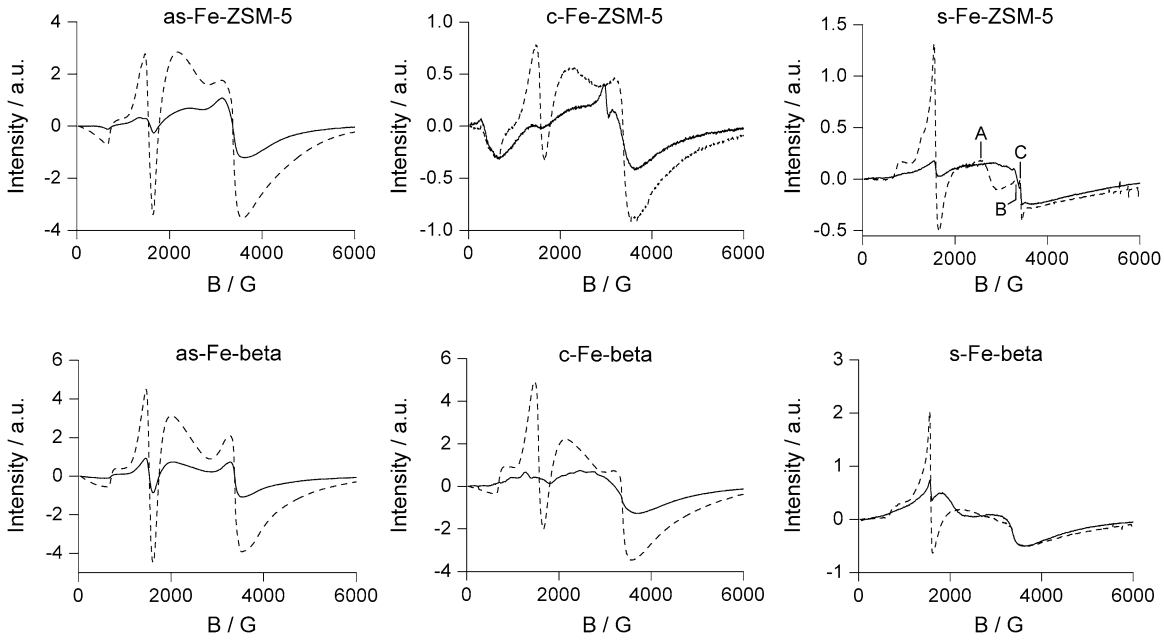

Fig. 13. EPR spectra of the as-synthesized, calcined, and steamed Fe-zeolites measured at 293 K (solid line) and 77 K (dashed line).

as a consequence of the higher concentration of dislodged (reducible) iron species. The increase in light absorption in the range above 600 nm can be attributed to an intervalence $Fe^{2+} \rightarrow Fe^{3+}$ CT transition characteristic of partially reduced Fe_3O_4-type clusters [74]. This indicates a preferential H_2 reduction of Fe^{3+} in iron oxide clusters.

Subsequent treatment of the reduced samples in air reoxidizes isolated iron species completely (Fig. 12). However, the band intensity above 400 nm in the steamed zeolites was not fully restored, indicating that a fraction of relatively large iron oxo-clusters and iron oxide particles remain in a reduced state after the second air treatment at 773 K. Curiously, the band intensity between 300 and 400 nm in c-Fe-beta is higher after reoxidation than before reduction. This is likely due to the agglomeration of a part of the isolated extra-framework Fe^{3+} sites into small oligonuclear clusters during the reduction treatment, which contribute to the band at 300–400 nm upon reoxidation. A similar irreversible agglomeration of isolated extra-framework sites was also observed by Kucherov et al. [75] by in situ EPR spectroscopy during reduction of Fe-ZSM-5 in a flow of 1 vol% H_2 in He at $T \geqslant 673$ K. Because of the higher iron content of their sample (4 wt% Fe), the formation of ferrimagnetic Fe_3O_4-type species was also observed.

3.8. EPR

The EPR spectra of the samples in Fig. 13 show signals at effective g' values of 2, 4.3, and 9, which have been found in a number of EPR studies on Fe-zeolites. However, the assignment of these signals to certain iron species is still a matter of controversy. Thus, the EPR signal at $g' \approx 2$ has typically been assigned to iron oxide clusters. However, isolated Fe^{3+} ions in positions of high symmetry (zero-field splitting parameters D, $E = 0$) also contribute to isotropic lines at $g' \approx 2$ [76,77]. Discrimination between the two cases may be possible by the temperature dependence and the line width of their EPR signals. Isolated, paramagnetic Fe^{3+} species show narrow signals that increase in intensity with falling temperature, whereas for iron oxide clusters broad lines are usually observed, the temperature dependence of which frequently deviates from paramagnetic behavior because of intrinsic antiferromagnetic interactions. The signal at $g' \approx 4.3$ and parts of the high-field spectrum at $g' \approx 9$ are frequently assigned to tetrahedrally coordinated Fe^{3+} ions in either framework [76,78,79] or extra-framework isolated positions [80–82], but the same line has also been attributed to isolated Fe^{3+} sites in octahedral symmetry [83]. As discussed previously [23,76,84], the position of the EPR signal of an isolated Fe^{3+} species in a powder spectrum depends just on the size and the ratio of the zero field splitting parameters D and E, which are a measure of the degree of site distortion but do not tell whether the Fe^{3+} species is tetradedrally or higher coordinated. This information, however, is accessible by UV/vis spectroscopy. Therefore, the combination of results from the two spectroscopies is particularly helpful for the identification of different Fe species.

HRTEM results (Fig. 10) for the as-synthesized zeolites do not point to any extra-framework Fe^{3+} species, and in the UV/vis spectra (Fig. 11) bands of isolated tetrahedral Fe^{3+} species are observed exclusively. On this basis, all EPR signals for as-Fe-ZSM-5 and as-Fe-beta can be assigned to tetrahedral Fe^{3+} ions in framework positions of high ($g' \approx 4.3$) and low ($g' \approx 2$) distortion. In the latter range, two signals are superimposed in the spectra of as-synthesized zeolites at 77 K, a narrow and a very broad one, both of which decrease upon heating, as expected for paramagnetic behavior (Fig. 13). The broad line might arise

from Fe^{3+} species with weak dipolar interactions that are not strictly isolated and feel the presence of each other, although they are not coupled by any magnetic long-range order. The two superimposed $g' \approx 2$ signals in the as-synthesized samples suggest that the tetrahedral Fe species are not homogeneously distributed in the zeolite lattice, leaving behind areas of low iron concentration with truly isolated Fe^{3+} sites and, in addition, areas with somewhat higher iron concentration in which weak dipolar interactions can occur.

Similar signals occur in the calcined zeolites (Fig. 13). However, for these materials UV/vis spectra indicate the creation of isolated octahedral Fe^{3+}, which might be located in extra-framework ion-exchange positions within the pores. Just from the EPR spectra this information is hardly derived, since the latter do not differ very much. Again, this illustrates that the position of the EPR signals alone cannot be used to draw conclusions about the coordination symmetry and the location in the zeolite matrix.

The spectrum of s-Fe-ZSM-5 at 77 K shows three superimposed signals in range of $g' \approx 2$ (A, B, and C), two of which exhibit nonparamagnetic behavior: a very broad one around $g' \approx 2.3$ (A) and one of 150 G peak-to-peak line width at $g' \approx 2$ (B). This suggests that Fe_2O_3 clusters of different sizes coexist in s-Fe-ZSM-5. A signal with a line width of 110 G that was resistant against reduction with H_2 at 873 K has been also observed in Fe-silicalite prepared by hydrothermal synthesis and containing ca. 0.7 wt% Fe [70]. This signal was assigned to superparamagnetic iron oxide particles outside the pores. Such species might be reflected by signal B in the s-Fe-ZSM-5 spectrum of Fig. 13. An additional rather narrow line (C) at $g' \approx 2$ was also identified, which decreases with increasing temperature, as expected for paramagnetic behavior. This signal is assigned to isolated Fe^{3+} species in high symmetry. It should be noted that its intensity is markedly smaller in the steamed sample as compared with the as-synthesized and calcined samples.

The spectrum of s-Fe-beta at room temperature shows also two very broad signals. One with a maximum around $g' \approx 4$ disappears upon cooling to 77 K, indicating effective antiferromagnetic coupling of the respective Fe centres at low temperature. Similar signals have also been observed in a liquid-ion exchanged Fe-beta sample with 1.9 wt% Fe [75]. The intensity of the second broad line around $g' \approx 2$ also does not increase upon cooling, which points to antiferromagnetic behavior. Thus, the two broad signals are likely related to oxidic clusters of different sizes, ranging from oligomeric moieties within the pores to extended Fe_2O_3-type particles at the external surface of the zeolite crystals. This is in agreement with the UV/vis results (Fig. 11), in which the formation of such species is indicated by several subbands above 300 nm. The signals at $g' \approx 4.3$ are markedly narrower in the steam-treated zeolites, as a consequence of the diminished dipolar interactions as a consequence of the massive extraction of iron to non-framework positions.

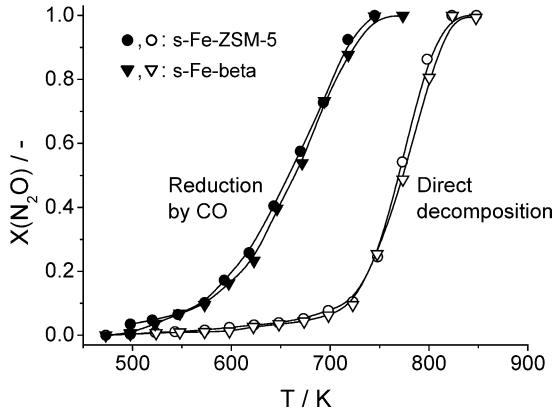

Fig. 14. N_2O conversion vs T during direct N_2O decomposition (1.5 mbar N_2O in He) and N_2O reduction by CO (1.5 mbar N_2O + 1.5 mbar CO in He) over s-Fe-ZSM-5 and s-Fe-beta. Conditions: W/F^0 (N_2O) = 3×10^5 g s mol^{-1} and $P = 1$ bar.

3.9. Catalytic activity

The performance of the steam-activated iron zeolites in direct N_2O decomposition and N_2O reduction by CO (Fig. 14) was primarily investigated to support conclusions derived from other characterization techniques and to examine the intrinsic influence of the zeolite matrix on catalytic activity. In these model reactions, it is well accepted that the nature and distribution of extra-framework iron species determine the N_2O conversion, whereas acidity (protons as Brønsted acids or extra-framework Al species as Lewis acids) plays a minor role [23,33,85]. As shown in the conversion versus temperature curves of Fig. 14, the activities of s-Fe-ZSM-5 and s-Fe-beta zeolites were very similar in the two catalytic processes. Both catalysts show significant conversion in direct decomposition above 700 K, which is complete at ca. 850 K. The required temperature for N_2O conversion over the steam-activated iron zeolites is reduced by ca. 150 K upon the addition of CO to the feed mixture, as a consequence of the accelerated removal of adsorbed atomic oxygen by the reducing agent [23]. We estimated the apparent activation energies (shown in Table 5) around the inflection (50% conversion) of the X versus T curves by assuming a plug-flow model and first-order reaction in N_2O. The values obtained for direct N_2O decomposition over both s-Fe-ZSM-5 and s-Fe-beta were very similar and significantly higher than those for N_2O reduction by CO. The absolute values of E_a^{app} and the trend upon the addition of CO to the feed are in good agreement with previous kinetic studies over ion-exchanged Fe-ZSM-5 [86]. The fact

Table 5
Apparent activation energies of the steamed Fe-zeolites in direct N_2O decomposition and N_2O reduction by CO (cf. Fig. 14)

Sample	E_a^{app}, N_2O (kJ mol^{-1})	E_a^{app}, N_2O + CO (kJ mol^{-1})
s-Fe-ZSM-5	182	67
s-Fe-beta	175	70

that the activation energies obtained over the two catalysts were almost identical excludes any significant influence of intracrystalline diffusion limitations related to the different crystal size in the samples. A strong control of the reaction by transport through the zeolite crystals would induce a lower apparent activation energy in s-Fe-beta, with crystals twice as large as those in s-Fe-ZSM-5 (cf. Fig. 3).

The remarkably similar performance of the steamed samples in Fig. 14 makes it possible to draw important general conclusions related to the scope of the methodology investigated here for zeolite preparation. First, and further substantiating the UV/vis characterization in Section 3.7, the same forms of iron can be stabilized in the different microporous structures of ZSM-5 and beta (Fig. 1) under identical activation conditions (calcination at 823 K and steam treatment in 30 vol% H_2O in N_2 at 873 K). This implies that the intrinsic role of the zeolite on the performance is not decisive as long as the iron constitution hosted in the materials is alike. Previous works in the literature dealing with various N_2O conversions have shown a higher [38–40] or lower [87] catalytic activity of Fe-beta compared with Fe-ZSM-5, which is typically prepared by a liquid-ion exchange method. However, these studies did not include an extensive (comparative) characterization of the nature and distribution of iron species in the materials. Consequently, it could not be concluded whether the different performance was (i) an intrinsic effect of the zeolite matrix or (ii) a consequence of the different iron forms in the catalysts. For the first time, our results enabled to uncouple these two effects, since very similar iron constitutions in Fe-beta and Fe-ZSM-5 are achieved by isomorphous insertion of iron in the framework, followed by its dislodgment to active extra-framework positions. Achieving this can be troublesome for liquid-ion exchange methods like those in [38–40,87]. It can be envisioned that the preparation of iron zeolites by such a post-synthesis approach strongly depends on the pore size of the parent material. The relatively large pores in beta may favor the introduction of a larger fraction of iron in active ion-exchange positions as compared with the more limited accessibility of the smaller micropores in ZSM-5, leading to a higher concentration of (inactive) iron agglomerates at the external surface of the zeolite crystals.

The above discussion on the matrix effect is valid for reactions where the catalysis is dominated by the redox function caused by extra-framework iron species. The effect on numerous catalyzed reactions, where, in addition, the acidic properties of the zeolite material are of importance, will be further investigated.

4. Conclusions

A multiple-technique approach has been successfully applied to the investigation of the physicochemical changes in Fe-beta and Fe-ZSM-5 prepared by hydrothermal synthesis upon activation by calcination and steam treatment. The chemical compositions of the synthesized zeolites were very similar (Si/Al and Si/Fe ratios), making comparison of the two systems straightforward. The extraction of framework Al and Fe heteroatoms during activation depends on the zeolite structure. Fe-beta is extensively dealuminated during thermal treatment for template removal, whereas the Al coordination is hardly changed upon calcination of Fe-ZSM-5. Extensive dealumination of the latter zeolite requires steam treatment at relatively high temperature. In contrast, the sensitivity of framework iron to migration into non-framework positions during post-synthesis treatments, as well as the nature and distribution of the resulting iron species, was remarkably alike for the two zeolite matrices. The remarkably similar catalytic performance of the steam-activated iron zeolites in direct N_2O decomposition and N_2O reduction with CO correlates well with the similar active forms of iron in the zeolites, regardless of the matrix (beta vs. ZSM-5) applied.

Acknowledgments

This research was financially supported by MCyT (PPQ 2002-01025) and DFG (grant no. Br1380/7-1). M.N.D. is indebted to AECI for a fellowship, and L.V. is grateful to MCyT for a Ramón y Cajal contract. Dr. P.J. Kooyman (TUDelft) and T. Bach (Hydro) are acknowledged for conducting the HRTEM and SEM analyses. We are indebted to Reviewer number 2 for the thorough evaluation and valuable comments on our original manuscript.

References

[1] J. Pérez-Ramírez, F. Kapteijn, G. Mul, J.A. Moulijn, Chem. Commun. (2001) 693.
[2] J. Pérez-Ramírez, F. Kapteijn, G. Mul, J.A. Moulijn, Appl. Catal. B 35 (2002) 227.
[3] J.A.Z. Pieterse, S. Booneveld, R.W. van den Brink, Appl. Catal. B 51 (2004) 215.
[4] H.Y. Chen, W.M.H. Sachtler, Catal. Today 42 (1998) 73.
[5] M. Kogel, R. Monnig, W. Schwieger, A. Tissler, T. Turek, J. Catal. 182 (1999) 470.
[6] R.Q. Long, R.T. Yang, J. Catal. 201 (2001) 145.
[7] G. Delahay, M. Mauvezin, A. Guzmán-Vargas, B. Coq, Catal. Commun. 3 (2002) 385.
[8] G.I. Panov, Cattech 4 (2000) 18.
[9] J. Jia, K.S. Pillai, W.M.H. Sachtler, J. Catal. 221 (2004) 119.
[10] A. Ribera, I.W.C.E. Arends, S. de Vries, J. Pérez-Ramírez, R.A. Sheldon, J. Catal. 195 (2000) 287.
[11] J. Pérez-Ramírez, E.V. Kondratenko, Chem. Commun. (2003) 2152.
[12] Q. Kan, Z. Wu, R. Xu, X. Liu, S. Peng, J. Mol. Catal. 74 (1992) 223.
[13] R.Q. Long, R.T. Yang, J. Catal. 201 (2001) 145.
[14] G. Ovejero, J.L. Sotelo, F. Martínez, J.A. Melero, L. Gordo, Ind. Eng. Chem. Res. 40 (2001) 3921.
[15] N. Narender, P. Srinivasu, S.J. Kulkarni, K.V. Raghavan, Stud. Surf. Sci. Catal. 135 (2001) 3745.
[16] P. Marturano, A. Kogelbauer, R. Prins, Stud. Surf. Sci. Catal. 125 (1999) 619.
[17] R. Joyner, M. Stockenhuber, J. Phys. Chem. B 103 (1999) 5963.

[18] F. Heinrich, C. Schmidt, E. Löffer, M. Menzel, W. Grünert, J. Catal. 212 (2002) 157.
[19] E.-M. El-Malki, R.A. van Santen, W.M.H. Sachtler, J. Catal. 196 (2000) 212.
[20] P. Kubánek, B. Wichterlová, Z. Sobalík, J. Catal. 211 (2002) 109.
[21] J. Pérez-Ramírez, F. Kapteijn, J.C. Groen, A. Doménech, G. Mul, J.A. Moulijn, J. Catal. 214 (2003) 33.
[22] J. Pérez-Ramírez, F. Kapteijn, A. Brückner, J. Catal. 218 (2003) 234.
[23] J. Pérez-Ramírez, M.S. Kumar, A. Brückner, J. Catal. 223 (2004) 13.
[24] M. Yoshida, T. Nobukawa, S. Ito, K. Tomishige, K. Kunimori, J. Catal. 223 (2004) 454.
[25] M.S. Kumar, M. Schwidder, M. Grünert, A. Brückner, J. Catal. 227 (2004) 384.
[26] W.K. Hall, X. Feng, J. Dumesic, R. Watwe, Catal. Lett. 52 (1998) 13.
[27] P. Marturano, L. Drozdová, A. Kogelbauer, R. Prins, J. Catal. 190 (2000) 460.
[28] A. Zecchina, S. Bordiga, G. Spoto, A. Damin, G. Berlier, F. Bonino, C. Prestipino, C. Lamberti, Top. Catal. 21 (2002) 67.
[29] J. Pérez-Ramírez, G. Mul, F. Kapteijn, J.A. Moulijn, A.R. Overweg, A. Doménech, A. Ribera, I.W.C.E. Arends, J. Catal. 207 (2002) 113.
[30] K.A. Dubkov, N.S. Ovanesyan, A.A. Shteinman, E.V. Starokon, G.I. Panov, J. Catal. 207 (2002) 341.
[31] G. Berlier, G. Spoto, S. Bordiga, G. Ricchiardi, P. Fisicaro, A. Zecchina, I. Rossetti, E. Selli, L. Forni, E. Giamello, C. Lamberti, J. Catal. 208 (2002) 64.
[32] A.M. Ferreti, C. Oliva, L. Forni, G. Berlier, A. Zecchina, C. Lamberti, J. Catal. 208 (2002) 83.
[33] J. Pérez-Ramírez, J. Catal. 227 (2004) 512.
[34] S. Bordiga, R. Buzzoni, F. Geobaldo, C. Lamberti, E. Giamello, A. Zecchina, G. Leofanti, G. Petrini, G. Tozzola, G. Vlaic, J. Catal. 158 (1996) 486.
[35] L.V. Pirutko, A.K. Uriarte, V.S. Chernyavsky, A.S. Kharitonov, G.I. Panov, Micropor. Mesopor. Mater. 48 (2001) 345.
[36] L.V. Pirutko, V.S. Chernyavsky, A.K. Uriarte, G.I. Panov, Appl. Catal. A 227 (2002) 143.
[37] G. Berlier, M. Pourny, S. Bordiga, G. Spoto, A. Zecchina, C. Lamberti, J. Catal. 229 (2005) 45.
[38] A. Guzmán-Vargas, G. Delahay, B. Coq, Appl. Catal. B 42 (2003) 369.
[39] M. Mauvezin, G. Delahay, F. Kisslich, B. Coq, S. Kieger, Catal. Lett. 62 (1999) 41.
[40] S. Kameoka, T. Suzuki, K. Yuzaki, T. Takeda, S. Tanaka, S. Ito, T. Miyadera, K. Kunimori, Chem. Commun. (2000) 745.
[41] G. Delahay, M. Mauvezin, B. Coq, S. Kieger, J. Catal. 202 (2001) 156.
[42] M. Mauvezin, G. Delahay, B. Coq, S. Kieger, J.C. Jumas, J. Olivier-Fourcade, J. Phys. Chem. B 105 (2001) 928.
[43] E.A. Zhilinskaya, G. Delahay, M. Mauvezin, B. Coq, A. Aboukaies, Langmuir 19 (2003) 3596.
[44] G. Mul, M.W. Zandbergen, F. Kapteijn, J.A. Moulijn, J. Pérez-Ramírez, Catal. Lett. 93 (2004) 113.
[45] Database of Zeolite Structures: http://www.iza-structure.org/databases.
[46] B.C. Lippens, J.H. de Boer, J. Catal. 4 (1965) 319.
[47] S. Brunauer, P.H. Emmet, E. Teller, J. Am. Chem. Soc. 60 (1938) 309.
[48] M.A. Camblor, A. Corma, S. Valencia, J. Mater. Chem. 8 (1998) 2137.
[49] G. Engelhard, D. Michel, High-Resolution Solid-State NMR of Silicates and Zeolites, Wiley, New York, 1987.
[50] M. Müller, G. Harvey, R. Prins, Micropor. Mesopor. Mater. 34 (2000) 135.
[51] P.B. Bodart, J.B. Nagy, G. Debras, Z. Gabelica, P.A. Jacobs, J. Phys. Chem. 90 (1986) 5183.
[52] J.L. Motz, H. Heinichen, W.F. Hölderich, J. Mol. Catal. A. Chem. 136 (1998) 175.
[53] A. Omegna, M. Haouas, A. Kogelbauer, R. Prins, Micropor. Mesopor. Mater. 46 (2001) 177.
[54] J.A. van Bokhoven, D.C. Koningsberger, P. Kunkeler, H. van Bekkum, A.P.M. Kentgens, J. Am. Chem. Soc. 122 (2000) 12842.
[55] A.E.W. Beers, J.A. van Bokhoven, K.M. de Lathouder, F. Kapteijn, J.A. Moulijn, J. Catal. 218 (2003) 239.
[56] A. Omegna, M. Vasic, J.A. van Bokhoven, G. Pirngruber, R. Prins, Phys. Chem. Chem. Phys. 6 (2004) 447.
[57] K.S.W. Sing, D.H. Everett, R.A.W. Haul, L. Moscou, R.A. Pierotti, J. Rouquerol, T. Siemieniewska, Pure Appl. Chem. 57 (1985) 603.
[58] F. Rouquerol, J. Rouquerol, K.S.W. Sing, in: F. Schütz, K.S.W. Sing, J. Weitkamp (Eds.), Handbook of Porous Materials, vol. 1, Wiley–VCH, Weinheim, 2002, p. 250.
[59] J.C. Groen, L.A.A. Peffer, J. Pérez-Ramírez, Micropor. Mesopor. Mater. 60 (2003) 1.
[60] R.J. Gorte, Catal. Lett. 62 (1999) 1.
[61] M.V. Juskelis, J.P. Slanga, T.G. Roberi, A.W. Peters, J. Catal. 138 (1992) 391.
[62] G. Busca, Phys. Chem. Chem. Phys. 1 (1999) 723.
[63] E.P. Parry, J. Catal. 2 (1963) 371.
[64] R. Buzzoni, S. Bordiga, G. Ricchiardi, C. Lamberti, A. Zecchina, G. Bellussi, Langmuir 12 (1996) 930.
[65] O.M. Busch, W. Brijoux, S. Thomson, F. Schüth, J. Catal. 222 (2004) 174.
[66] T.R. Hughes, H.M. White, J. Phys. Chem. 71 (1967) 2192.
[67] E.R.A. Matulewicz, F.R.J.M. Kerkhof, J.A. Moulijn, H.J. Reitsma, J. Colloid Interface Sci. 77 (1980) 110.
[68] P.A. Jacobs, C.F. Heylen, J. Catal. 34 (1974) 267.
[69] E. Selli, I. Forni, Micropor. Mesopor. Mater. 31 (1999) 129.
[70] D. Meloni, R. Monaci, V. Solinas, G. Berlier, S. Bordiga, I. Rossetti, C. Oliva, L. Forni, J. Catal. 214 (2003) 169.
[71] G. Lehmann, Z. Phys. Chem. Neue Folge 72 (1970) 279.
[72] A.A. Akl, Appl. Surf. Sci. 233 (2004) 307.
[73] H.H. Tippins, Phys. Rev. B 1 (1969) 126.
[74] J. Tang, M. Myers, K.A. Bosnick, L.E. Brus, J. Phys. Chem. B 107 (2003) 7501.
[75] A.V. Kucherov, C.N. Montreuil, T.N. Kucherova, M. Shelev, Catal. Lett. 56 (1998) 181.
[76] A. Brückner, U. Lohse, H. Mehner, Micropor. Mesopor. Mater. 20 (1998) 207.
[77] G. Catana, J. Pelgrims, R.A. Schoonheydt, Zeolites 15 (1995) 475.
[78] P.N. Joshi, S.V. Awate, V.P. Shiralkar, J. Phys. Chem. 97 (1993) 9749.
[79] T. Inui, H. Nagata, T. Takeguchi, S. Iwamoto, H. Matsuda, M. Inoue, J. Catal. 139 (1993) 482.
[80] D. Goldfarb, M. Bernardo, K.G. Strohmaier, D.E.W. Vaughan, H. Thomann, J. Am. Chem. Soc. 116 (1994) 6344.
[81] A.V. Kucherov, A.A. Slinkin, Zeolites 8 (1988) 110.
[82] B. Wichterlová, P. Jiru, React. Kinet. Catal. Lett. 13 (1980) 197.
[83] J.W. Park, H. Chon, J. Catal. 133 (1992) 159.
[84] R. Aasa, J. Chem. Phys. 52 (1983) 3919.
[85] J. Pérez-Ramírez, F. Kapteijn, G. Mul, J.A. Moulijn, Catal. Commun. 3 (2002) 19.
[86] F. Kapteijn, G. Marbán, J. Rodríguez-Mirasol, J.A. Moulijn, J. Catal. 167 (1997) 256.
[87] J. Pérez-Ramírez, F. Kapteijn, G. Mul, J.A. Moulijn, J. Catal. 208 (2002) 211.